JBC RESEARCH ARTICLE

Free ferrous ions sustain activity of mammalian stearoyl-CoA desaturase-1

Received for publication, April 14, 2023, and in revised form, May 26, 2023 Published, Papers in Press, June 7, 2023,
https://doi.org/10.1016/j.jbc.2023.104897

Jiemin Shen[1], **Gang Wu**[2,*], **Brad S. Pierce**[3], **Ah-Lim Tsai**[2,*], **and Ming Zhou**[1,*]

From the [1]*Verna and Marrs McLean Department of Biochemistry and Molecular Biology, Baylor College of Medicine, Houston, Texas, USA;* [2]*Department of Internal Medicine, University of Texas McGovern Medical School, Houston, Texas, USA;* [3]*Department of Chemistry & Biochemistry, University of Alabama, Tuscaloosa, Alabama, USA*

Reviewed by members of the JBC Editorial Board. Edited by Joan B. Broderick

Mammalian stearoyl-CoA desaturase-1 (SCD1) introduces a double-bond to a saturated long-chain fatty acid in a reaction catalyzed by a diiron center. The diiron center is well-coordinated by conserved histidine residues and is thought to remain with the enzyme. However, we find here that SCD1 progressively loses its activity during catalysis and becomes fully inactive after about nine turnovers. Further studies show that the inactivation of SCD1 is due to the loss of an iron (Fe) ion in the diiron center and that the addition of free ferrous ions (Fe^{2+}) sustains the enzymatic activity. Using SCD1 labeled with Fe isotope, we further show that free Fe^{2+} is incorporated into the diiron center only during catalysis. We also discover that the diiron center in SCD1 has prominent electron paramagnetic resonance signals in its diferric state, indicative of distinct coupling between the two ferric ions. These results reveal that the diiron center in SCD1 is structurally dynamic during catalysis and that labile Fe^{2+} in cells could regulate SCD1 activity and hence lipid metabolism.

Stearoyl-CoA desaturases (SCDs) are redox-active diiron enzymes embedded in the membrane of endoplasmic reticulum (1–3). SCDs catalyze the conversion of saturated fatty acids to monounsaturated fatty acids (MUFAs) (3). Human has two SCD isoforms (SCD1 and SCD5) (4), while mouse has four (SCD1-4) that are the co-orthologs of human SCD1 (5). Studies have shown that mice with SCD1 knocked out are resistant to high-fat diets (6, 7) and that SCD1 activity is crucial for maintaining the balance between fat consumption and accumulation (8). Inhibition of SCD1 has been pursued to treat metabolic diseases such as obesity and diabetes (3, 6, 7, 9–15). SCD-mediated desaturation is the major route for the *de novo* synthesis of MUFAs, which is essential for cell survival (16–19). Elevated expression of SCD1 has been observed in various types of cancer cells (20), and the high level of MUFA production by SCD1 protects cancer cells against ferroptosis (21–23). Preclinical studies of SCD1 inhibitors have shown benefits for the treatment of cancers (19, 24–29). SCD1 is also a promising target for reversing the pathology in neurodegenerative diseases, such as Parkinson's and Alzheimer's diseases (30–33).

SCDs have a diiron center that undergoes oxidation during the catalysis (3) and is recovered by reducing equivalents delivered by a heme protein cytochrome b_5 (cyt b_5) (34). Cyt b_5 receives electrons from cytochrome b_5 reductase (b_5R), which obtains electrons from reduced NADH *via* a bound flavin adenine dinucleotide (FAD) cofactor (35–39). The three proteins, b_5R, cyt b_5, and SCD1, form an endoplasmic reticulum–resident electron transfer chain that sustains the desaturation reaction with NADH oxidation and molecular oxygen (O_2) reduction (3) (Fig. 1*A*). SCDs have four transmembrane (TM) helices (40–42), while both b_5R and cyt b_5 have a single TM helix (34, 39). In a recent study, we found that the three proteins form a stable ternary complex mediated mainly by the TM helices and that the formation of a stable ternary complex accelerates electron transfer (43).

Initial structures of SCD1s have a diiron center that was misincorporated with two zinc ions (Zn^{2+}), an artifact likely stemmed from overexpression of the proteins in insect cells (41, 42). In a follow-up study, we developed a protocol to produce mammalian SCD1 with >90% iron (Fe) occupancy and determined its crystal structure (44). These studies (41, 42, 44) defined a unique diiron center coordinated entirely by histidine residues: two Fe ions (Fe1 and Fe2) are coordinated by the imidazole side chain of nine histidine residues, five for Fe1, four for Fe2; the Fe···Fe distance is 6.4 Å. This configuration is different from previously resolved diiron centers (45–48), which contain carboxylate ligands with one or two carboxylates forming bidentate bridge(s) between the two Fe ions, restricting the Fe···Fe distance to less than 4 Å. The distinct configuration of the diiron center in SCD1 is representative of many membrane-bound desaturases and hydroxylases (47, 49, 50), but its reaction mechanism remains unclear (48). In this study, we report the catalytic inactivation of the diiron center in SCD1 and the regulation of SCD1 activity by exogenous ferrous ions (Fe^{2+}).

Results

Fast inactivation of SCD1

In a previous study, we purified Fe-loaded mouse SCD1 from human embryonic kidney (HEK) cells and verified its Fe

* For correspondence: Ming Zhou, mzhou@bcm.edu; Gang Wu, gang.wu@uth.tmc.edu; Ah-Lim Tsai, Ah-Lim.Tsai@uth.tmc.edu.

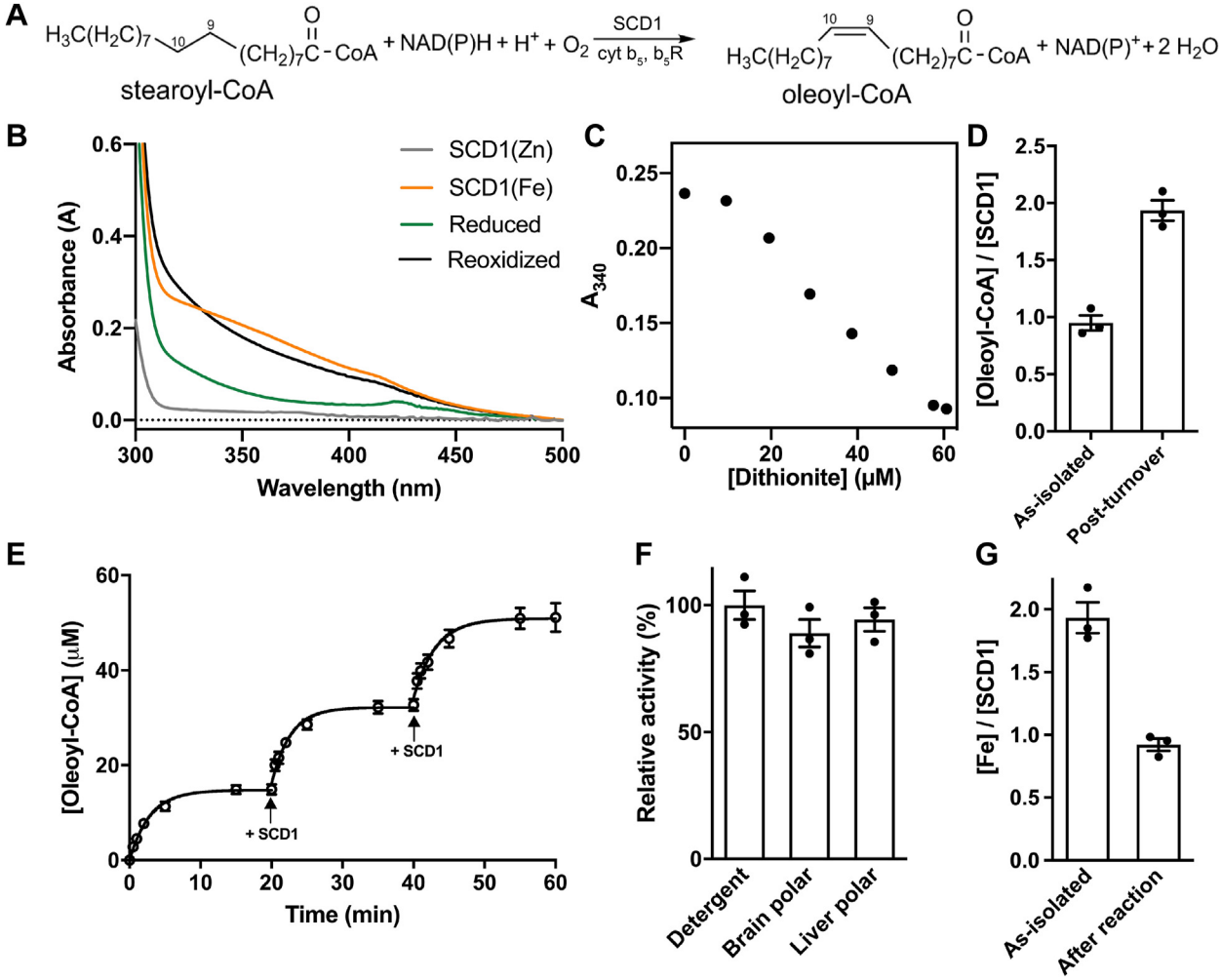

Figure 1. Single turnover and continuous turnover reaction of SCD1. *A*, overall reaction scheme of the biological desaturation by SCD1. The Δ9 and Δ10 carbons on the acyl chain are labeled. *B*, UV/Vis spectra of Zn-containing (*gray*), Fe-containing (*orange*), dithionite-reduced (*green*), and reoxidized (*black*) SCD1. *C*, anaerobic titration of dithionite into 50 μM as-isolated SCD1. *D*, molar ratios of oleoyl-CoA to SCD1 in samples before and after chemical reduction and reoxidation in the presence of substrate stearoyl-CoA. *E*, time course of oleoyl-CoA production by SCD1 in the biological pathway with cyt b_5 and b_5R. The same amount of SCD1 was added at time points indicated by *black arrows*. *F*, activities of SCD1 in detergent or in liposomes prepared with brain polar or liver polar lipids. *G*, Fe content analysis of SCD1 before and after reaction by ICP-MS. The molar ratios of Fe to protein are shown. In this paper, error bars represent the SEM from three repeats. ICP-MS, inductively coupled plasma mass spectrometry; SCD, stearoyl-CoA desaturase.

content in two ways (44). First, we measured Fe content using inductively coupled plasma mass spectrometry (ICP-MS) and found that the molar ratio of Fe:SCD1 is ∼2:1. Second, we verified the presence and location of the diiron center in the crystal structure by the anomalous X-ray dispersion signals of Fe. Here, we further characterized the diiron center. We chemically reduced the diiron center in the purified SCD1 by anaerobic stoichiometric titration with dithionite and monitored the decrease of absorbance of diferric cluster (Fe(III)/Fe(III)) at 340 nm (A_{340}) (Fig. 1*B*). We found that ∼2 reducing equivalents are required to fully reduce the diiron center in the purified SCD1 (Fig. 1*C*), which further confirms the 2:1 [Fe]:[SCD1] ratio, and indicates that the resting diiron center in purified SCD1 is in the Fe(III)/Fe(III) state. We then show that SCD1 reduced by dithionite is enzymatically active and produces one equivalent of product in the presence of stearoyl-CoA and O_2, indicative of a single turnover reaction (Fig. 1*D*).

We proceed to examine SCD1 activity under conditions that enable multiple turnovers. In the presence of purified mouse cyt b_5 and b_5R and sufficient amount of substrate stearoyl-CoA and NADH (1 mM), the formation of product oleoyl-CoA levels off with an average total turnover number (TTN) of 8.5 ± 0.3 (Fig. 1*E*). However, when fresh SCD1 is added to the reaction mixture, we observed additional product formation with almost identical initial rate and TTN to the initial round (Fig. 1*E*). And this process can be repeated with the same outcome. There seems to be a linear relationship between the amount of SCD1 and the yield of oleoyl-CoA, whether the enzyme is added in increments or all at the beginning (44). Thus, the loss of enzymatic activity is not due to the exhaustion of reducing equivalents or substrates nor is it due to product inhibition. We conclude that SCD1 becomes progressively self-inactivated after each turnover, and we surmise that this is due to the loss of Fe in SCD1.

To alleviate concern that detergent-solubilized SCD1 becomes unstable during the reaction, we conduct the following two experiments. First, we reconstitute purified SCD1 into liposomes for the enzymatic assay, and we observe a similar loss of activity as the reaction progresses (Fig. 1*F*). We also notice that in an earlier study of SCD1 from crude extract of liver microsomes, self-inactivation was obvious with a similar TTN (51). Second, we purified the inactivated SCD1 from the reaction mixtures by size-exclusion chromatography (SEC). A monodispersed peak in SEC (Fig. S1*A*) and a single band in SDS-PAGE (Fig. S1*B*) indicate that the inactivated SCD1 is biochemically stable as it was before the reaction. We conclude that the inactivation of SCD1 is not due to protein aggregation or loss of its lipidic environment.

Loss of SCD1 activity in the peroxide shunt pathway

Similar to cytochrome P450, diiron enzymes can react with hydrogen peroxide (H_2O_2) to drive enzymatic turnover in the absence of an electron transfer chain, which is referred to as the "peroxide shunt" pathway (48, 52). This pathway has not been reported in SCD1. We find that SCD1 can utilize the peroxide shunt pathway (Fig. S2*A*), although the rate of substrate formation is significantly slower (Fig. S2*B*). The K_M for H_2O_2 is 18.4 ± 2.3 mM and the k_{cat} is 0.84 ± 0.03 min^{-1} (Fig. S2*C*), which is ∼3.3-fold slower than the biological pathway. SCD1 also displays progressive loss of activity with a TTN of 6.8 ± 0.3, but over a longer period of time (∼30 min) (Fig. S2*B*). Although the peroxide shunt pathway may not be biologically relevant, it incurs a similar loss of enzymatic activity. This leads us to hypothesize that SCD1 activity is vulnerable to self-inactivation during the oxidation of the diiron center.

We also examined the kinetics of the peroxide shunt pathway in SCD1 by following the UV-Vis spectra of the diiron center after rapid mixing. The time course can be deconvoluted into two major phases (1 and 2) with transition rates of 9.7 s^{-1} and 0.17 s^{-1} (Fig. S2*D*), which reflect the reaction of the diiron center with H_2O_2. These rates are much faster than the k_{cat} of oleoyl-CoA production, suggesting that the H_2O_2 activation of the diiron center is not the rate-limiting step.

Loss of one Fe during catalysis

We measured the amount of Fe in the inactivated SCD1 by ICP-MS and found that the [Fe]:[protein] ratio drops from ∼2:1 to ∼1:1 (Fig. 1*G*). It is more likely that most of the SCD1 has lost a single Fe ion than the alternative interpretation that there is a mixture of SCD1 with zero, one, or two Fe ions. We will further examine the stoichiometry in the Fe exchange experiments and in electron paramagnetic resonance (EPR) analyses described later in the manuscript. We also found that the diiron center in the purified SCD1 is resistant to chelation by EDTA (Experimental procedures). We speculate that the loss of Fe occurs only during the catalytic cycle, likely when the diiron center experiences a higher oxidation state.

Exogenous Fe^{2+} enhances the activity of SCD1

We then examined the activity of SCD1 in the presence of free Fe^{2+} in the solution and found that Fe^{2+} can sustain the reaction as evidenced by significantly higher amount of substrate conversion (Fig. 2*A*). Other common transition metal ions were also tested, but none of them significantly changes the TTN of SCD1, including ferric ion (Fe^{3+}) (Fig. 2*B*). Ascorbate, added to protect Fe^{2+} from oxidation in solution, does not enhance the activity of TTN by itself (Fig. 2*B*). The enhancement by Fe^{2+} is concentration-dependent with a half maximal EC_{50} of 6.5 (4.5–9.4) μM (95% confidence interval in parentheses) (Fig. 2*C*). Further, we found that addition of free Fe^{2+} prior to the start of the reaction does not increase the initial rate of reaction (Fig. 2*D*, inset) but only increases the TTN in the reaction system. After SCD1 is inactivated, however, addition of Fe^{2+} does not recover the enzymatic activity (Fig. 2*E*), indicating that the protection of enzymatic activity by free Fe^{2+} occurs during the catalytic cycle.

Fe exchange occurs during catalysis

To further understand how free Fe^{2+} helps prevent the inactivation of SCD1, we prepared SCD1 samples enriched with ^{57}Fe to track changes of Fe in the diiron center (Experimental procedures). We first expressed and purified ^{57}Fe-enriched SCD1 (Experimental procedures) and recovered the ^{57}Fe-enriched SCD1 after ∼30 min reaction in the presence of free $^{56}Fe^{2+}$ in the solution. ICP-MS shows that while the total [Fe]:[protein] ratio is still close to 2:1 (Fig. 2*F*), the isotope composition changes dramatically: the endogenous [^{57}Fe] in SCD1 drops by ∼50%, and the exogenous [^{56}Fe] becomes comparable to [^{57}Fe], making the [^{56}Fe]:[^{57}Fe]:[protein] ratio close to unity (Fig. 2*F*). As expected, incubation of $^{56}Fe^{2+}$ with ^{57}Fe-enriched SCD1 for ∼1 h without initiating the catalysis does not allow the incorporation of $^{56}Fe^{2+}$ into the diiron center (Fig. S3), indicative of a stable diiron center at the resting state. We conclude that free (exogenous) Fe^{2+} is only able to replace the bound (endogenous) Fe during catalysis. Since SCD1 in the absence of free Fe^{2+} is fully inactivated after 30 min while SCD1 in the presence of Fe^{2+} remains fully active after 30 min (Fig. 2*D*), we conclude that the mixed isotope $^{57}Fe/^{56}Fe$ center is likely the dominant species in the SCD1 sample after the reaction.

Unique EPR signatures of resting SCD1

Since the diiron center in the purified SCD1 is in the Fe(III)/Fe(III) state, we proceed to examine the diiron center using EPR spectroscopy. Previous studies of the diiron centers in several enzymes show that they are EPR-silent in the Fe(III)/Fe(III) state due to the antiferromagnetic (AF) coupling of two Fe(III), likely *via* bridging ligand(s) (48). However, due to the long Fe···Fe separation (6.4 Å) and lack of a bridging ligands in SCD1, we consistently obtain EPR signals from SCD1. SCD1 has a sharp asymmetric species at g ∼4.3 (Fig. 3*A*, I) with a half-saturation power ($P_{1/2}$) of ∼141 mW (Fig. 3*B*), which is typical of highly rhombic high-spin Fe(III) EPR. Interestingly, SCD1 also has a prominent broad species with a linewidth of

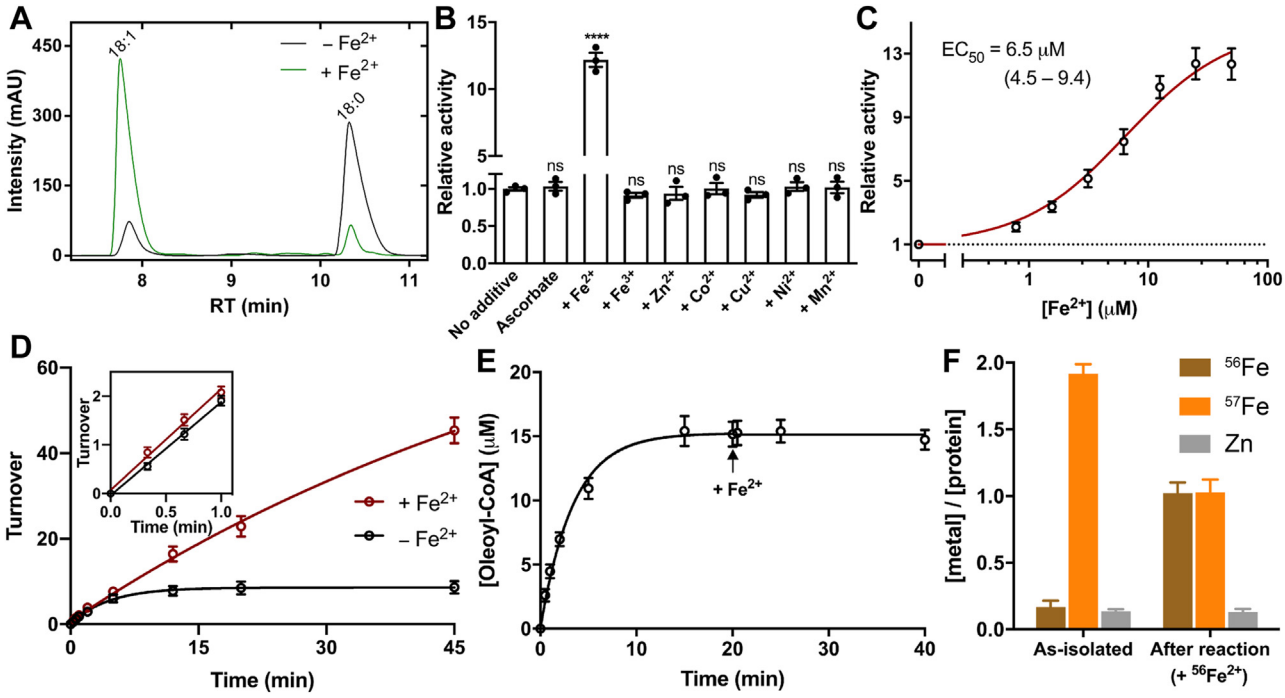

Figure 2. Enhanced activity of SCD1 in the presence of exogenous Fe^{2+}. *A*, HPLC profiles of acyl-CoA conversions in the absence (*black*) or presence (*green*) of Fe^{2+}. Peaks for the product (18:1) and substrate (18:0) are labeled. *B*, activities of SCD1 in the presence of exogenous transition metal ions. Statistical significances were analyzed with one-way ANOVA followed by Dunnett's test for multiple comparisons. ns, not significant; ****$p < 0.0001$. *C*, concentration-dependent potentiation of SCD1 activity by exogenous Fe^{2+}. The EC_{50} value was calculated from the fit (*red line*) to an excitatory dose-response equation. The reactions were performed with 1 μM SCD1, and 1 mM ascorbate-Na was added together with Fe^{2+}. *D*, time courses of oleoyl-CoA production in the presence (*red*) or absence (*black*) of exogenous Fe^{2+}. The inset shows that the initial rates are not significantly different in the two conditions. *E*, no additional product formation after the addition of Fe^{2+} (*black arrow*) to inactivated SCD1. No exogenous Fe^{2+} was present prior to the start of reaction. *F*, metal content analysis of ^{57}Fe-enriched SCD1 before and after reaction. $^{56}Fe^{2+}$ was added prior to the start of reaction. SCD1 was separated for analysis after 30 min reaction. SCD, stearoyl-CoA desaturase.

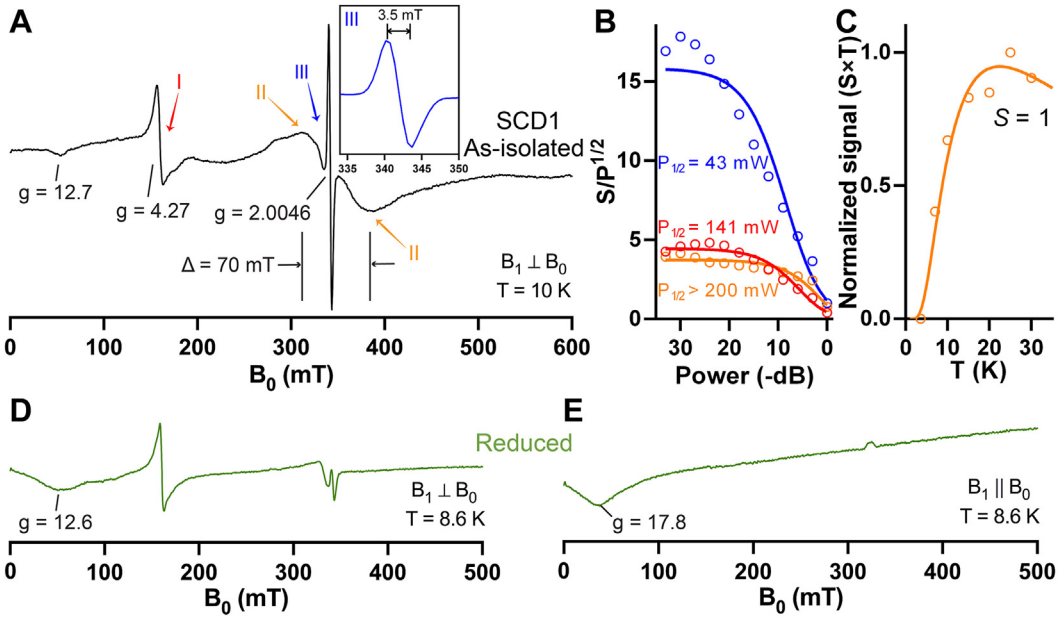

Figure 3. EPR spectroscopy of the diiron center in SCD1. *A*, as-isolated SCD1 (1 mM) at 10 K shows strong EPR signals around $g = 4$ to 6 (I), a broad symmetric signal centered at $g \sim 2$ with a peak-to-trough span (Δ) = 70 mT (II), and a sharp radical-like signal (III). Inset: Narrow field window of EPR species III (*blue*). *B*, power dependence of EPR species I (*red*), II (*orange*), and III (*blue*) at 10 K. *C*, the temperature dependence of the normalized signal of species II from $S = 1$ (*orange circles*) and the calculated Boltzmann curve (*orange line*). EPR spectrum of SCD1 after photoreduction (*green*) in perpendicular mode (*D*) or in parallel mode (*E*). EPR, electron paramagnetic resonance; SCD, stearoyl-CoA desaturase.

~70 mT centered at nominal g ~2.0 (Fig. 3*A*, II). Species II relaxes extremely efficient with a $P_{1/2}$ higher than 200 mW (Fig. 3*B*). Crucially, the temperature dependence of II does not follow Curie's Law behavior. Instead, the temperature-normalized signal intensity (S × T) increases with temperature, indicating that an excited "EPR-active" spin manifold is being populated. This observation is inconsistent with the behavior expected for known (S = 1/2) mixed valent Fe(II)/Fe(III) or Fe(III)/Fe(IV) clusters. While much more work is needed to assign this specific EPR transition, the observed temperature dependence of II can be modeled as a transition within an excited S = 1 manifold assuming weak (J = −7.5 cm^{-1}) AF coupling of two high spin Fe(III) sites. If correct, the magnitude of this AF coupling would be the lowest reported among enzymatic Fe(III)/Fe(III) clusters (48). Additional work and quantitative simulations are needed to fully validate this assignment.

Results presented above are consistent with the conclusion that EPR species II originates from a weakly coupled Fe(III)/Fe(III) cluster in resting SCD1 through a mechanism currently under investigation. Significantly, this broad EPR species is not observed in samples prepared from His265Leu SCD1. This SCD1 variant has a crippled Fe2-binding site (see below) and thus cannot produce a diiron cluster.

Apart from the broad species II, multiple batches of SCD1 exhibit a consistent narrow EPR signal centered at g ~2.0 (Fig. 3*A*, III). This feature has a linewidth of ~3.5 mT with an isotropic lineshape (Fig. 3*A*, inset). The g-value and narrow linewidth of the species suggests an organic radical. However, as shown in Figure 3*B*, the power required for half-saturation ($P_{1/2}$, 43 mW) is significantly higher than that typically observed for organic radicals. The fast relaxation observed for species III suggests that it is likely close to another paramagnetic center, presumably the coupled diiron center.

The EPR spectrum of SCD1 has significant changes upon reduction. Photoreduction that converts the diiron center to the diferrous (Fe(II)/Fe(II)) state largely eliminates EPR signals II and III (Fig. 3*D*). The fully reduced Fe(II)Fe(II) diiron cluster can be observed in the perpendicular mode (9.58 GHz) EPR spectra as a weak dip with the trough centered at an apparent g-value of ~13. This cluster is more readily observed by switching to parallel mode (9.23 GHz) where the Fe(II)Fe(II) cluster exhibits a characteristic signal near g ~18 (Fig. 3*E*).

Single turnover of SCD1 with cyt b_5 and b_5R monitored by EPR

We then examined redox-dependent changes of the EPR signals from SCD1 when reacted with its physiological electron transfer partner cyt b_5, which is in turn reduced by b_5R using NADH. To ensure efficient electron transfer, we used a stable ternary complex composed of SCD1, full-length cyt b_5, and b_5R reported previously (43). The EPR spectrum (at 10 K) of the resting state complex shows distinguishable signatures from low-spin heme Fe(III) of cyt b_5 at g ~2.17 and g ~3.05 (53) and from SCD1 at g ~4.3, g ~2.1, and g ~2.0 (Fig. S4*A*). SCD1 in the ternary complex exhibits similar EPR signatures as the individual SCD1. We then added an equal molar amount of NADH to the complex and followed redox changes by freeze quench. After 10 s, the g ~2.0 signal intensifies dramatically, which has a linewidth of only ~1.5 mT, consistent with an anionic FAD semiquinone radical ($FAD^{-}\cdot$) (38) in b_5R. The $FAD^{-}\cdot$ is generated from the rapid hydride transfer from NADH to FAD in b_5R and subsequent one-electron transfer from $FADH_2$ to cyt b_5 and O_2 (Fig. S4*D*). The disappearance of the heme Fe(III) signals marks the full reduction of cyt b_5 (Fig. S4*C*). Moreover, the g ~2.1 signal from SCD1 starts to decrease, reflecting the fast electron transfer from cyt b_5 to the diiron center (Fig. S4*B*). After another 30 s, the g ~4.3 signal from SCD1, which stays almost unchanged after 10 s reaction, starts to drop (Fig. S4*B*), suggesting relatively slower reduction kinetics. While the signal of $FAD^{-}\cdot$ disappears within ~160 s (Fig. S4*D*), signals from cyt b_5 and SCD1 gradually recover over ~30 min due to slow reoxidation of the heme and diiron center by O_2 (Fig. S4*B* and *C*). Compared to the g ~2.1 signal, the g ~4.3 signal has a slower reoxidation rate (Fig. S4*B*). These observations support our assignment of the peaks in the EPR spectrum of SCD1 and establish EPR spectroscopy as a powerful approach for further investigation of the mechanism of the diiron center.

Loss of Fe2 in SCD1

EPR spectrum provides an independent way of assessing the loss of Fe in SCD1. EPR spectra collected on inactivated SCD1 exhibit multiple signals, which can be attributed to high-spin Fe(III). In addition to the sharp g ~4.3 signal attributed to a transition within the middle doublet (m_s = ±3/2) of the high-spin state, weaker signals are also observed at g-values ranging from 5 to 9 (Fig. 4*A*). Significantly, the broad species II and the sharp species III found in the fully active SCD1 are not observed in the inactivated SCD1. These observations, combined with the ICP-MS result, support our hypothesis that the inactivated SCD1 is predominantly bound with a single Fe in the diiron center.

To further identify which Fe is lost from SCD1, we mutated each of the nine Fe-coordinating histidine residues to leucine. However, out of the nine histidine-to-leucine point mutations, only His265Leu that coordinates Fe2 is biochemically stable and has sufficient yield for EPR study (Fig. S5*A*). The Fe occupancy of His265Leu SCD1 is slightly less than one iron per SCD1 (Fig. S5*B*) and it does not have enzymatic activity. His265Leu SCD1 has EPR signals at g-values from 5 to 9 and ~4.3 (Fig. 4*A*), but no broad species II and sharp species III were observed in the WT SCD1. Compared with WT SCD1, the saturation behavior ($P_{1/2}$, 29 mW) of His265Leu SCD1 variant is much lower (Fig. 4*B*). This is likely attributed to the absence of the adjacent Fe2 ion, as the presence of a nearby paramagnetic center would increase spin relaxation, leading to higher $P_{1/2}$. These features in the EPR spectrum of His265Leu are consistent with a crippled diiron center singly occupied at Fe1 (Fig. 4*C*). Similar EPR signatures of the inactivated SCD1 and the His265Leu SCD1 imply that Fe2 is lost during the catalysis, although we cannot fully exclude the possibility of

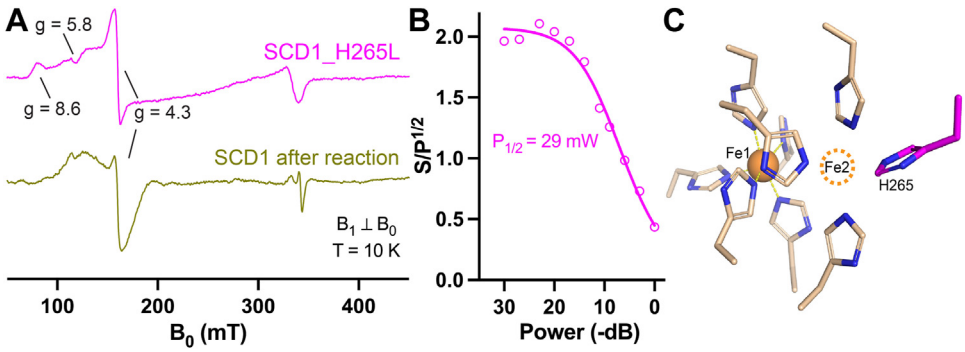

Figure 4. Loss of Fe detected by EPR spectroscopy. *A*, comparison of EPR spectra of SCD1 with H265L mutation (*magenta*), 850 μM; SCD1 after catalytic inactivation (*yellow*), 800 μM. *B*, power dependence of EPR signals of H265L at 10 K. *C*, structure of the diiron center in SCD1 (PDB ID: 6WF2), showing nine histidine residues in the first coordination sphere. Fe2 is drawn as an *orange dashed circle*. H265 is highlighted in *magenta*. EPR, electron paramagnetic resonance; PDB, Protein Data Bank; SCD, stearoyl-CoA desaturase.

loss of Fe1 due to the lack of EPR spectra from SCD1 singly occupied with Fe2.

Discussion

In summary, we found that SCD1 catalyzes on average ∼8.5 cycles of the desaturation reaction before fully inactivated and that the inactivation is caused by the loss of one Fe, most likely Fe2, in the diiron center. The presence of free Fe^{2+} in solution can replace the lost Fe during the enzymatic reaction and thus alleviates or prevents inactivation. However, Fe^{2+} is not able to revive SCD1 once it has already been inactivated. These behaviors were not reported in any other diiron enzymes and seem unique to SCD1 and, by extension, to membrane-bound desaturases that contain a similar diiron center, such as fatty acid desaturase (FADS2) and sphingolipid Δ4-desaturase-1 (DES1) (Fig. S6).

We notice that the purified SCD1 has a bound oleoyl-CoA (Fig. 1*D*), indicative of a rate-limiting step in product release. It is possible that the loss of one Fe could occur during product release, which requires structural changes. Alternatively, if a highly reactive species is generated in SCD1, for example, $Fe(IV)=O^{2-}$ (54), it may irreversibly damage surrounding residues (55, 56) such as the histidine residues that coordinate Fe2. The damage may be prevented in the presence of free Fe^{2+}. Self-inactivation was observed in prostaglandin H-synthase, and the culprit is likely the ferryl heme intermediate rather than the active tyrosyl radical (57). In nitric oxide synthase, when either the substrate or the tetrahydrobiopterin cofactor is absent, the P450-like heme can generate superoxide and H_2O_2 reactive oxygen species and alter the reaction from nitric oxide synthesis to superoxide (or H_2O_2 or even peroxynitrite) synthesis (58, 59). Without a bridging ligand between the two Fe ions, the increased structural flexibility may enhance such damaging side reactions to inactivate the enzyme when a high oxidation state or peroxo intermediate is formed.

We report the first EPR spectrum of the diiron center in SCD1. Distinct from other well-characterized soluble diiron enzymes, such as ribonucleotide reductase, soluble methane monooxygenase, and acyl-acyl carrier protein desaturase, SCD1 in the resting state has a broad EPR species which likely comes from coupled Fe1 and Fe2. The assignment of this EPR signature is supported by its disappearance in the His265Leu mutant and inactivated SCD1 (Fig. 4*A*), both of which contain only one Fe. This EPR signature is also sensitive to changes in the redox state, as observed in chemically reduced SCD1 (Fig. 3, *D* and *E*) as well as in the biological pathway with cyt b_5 and b_5R (Fig. S4). The EPR of SCD1 also shows a radical signal at g ∼2.0, which suggests that a high-valent Fe could generate an amino acid radical(s) in its vicinity. We anticipate that refined assignments of the rich EPR signatures of SCD1 will help gain insights into the electronic structure and reactivity of the unique diiron center in the future.

The enhancement of the desaturation activity of SCD1 is dependent on the concentration of free Fe^{2+} in solution. The EC_{50} (6.5 μM) of the potentiation by Fe^{2+} is relevant to typical Fe concentration (∼2 μM) in the cellular labile iron pool (60, 61), which includes Fe^{2+} in complex with chelators such as glutathione and ascorbate. Thus, labile iron pool could be a regulatory factor of SCD1 activity.

Experimental procedures

Expression and purification of SCD1 and related proteins

The codon-optimized complementary DNA of N-terminal truncated mouse SCD1 (Δ2–23) and full-length human SCD5 were cloned into pEG BacMam vectors with a C-terminal enhanced green fluorescent protein (eGFP) tag. Expression was performed through transduction of HEK 293S cells with baculoviruses produced in Sf9 (*Spodoptera frugiperda*) cells following the standard BacMam protocol (62) as previously reported. *FreeStyle 293* media (Invitrogen/Thermo Fisher Scientific) were supplemented with apo-transferrin (Athens Research & Technology) and $FeCl_3$ (Sigma). Ten millimolar sodium butyrate (Sigma) was added 1 day after viral transduction, and the temperature was lowered from 37 to 30 °C. For expression of SCD1–cyt b_5–b_5R ternary complex, 0.5 mM δ-aminolevulinic acid (Santa Cruz) and 100 μM riboflavin (Sigma) were added to the media to enhance the incorporation of heme and FAD, respectively. Cell membranes were solubilized with 30 mM n-dodecyl-β-D-maltopyranoside (Anatrace).

Homemade eGFP nanobody-conjugated resins (NHS-Activated Sepharose 4 Fast Flow, Cytiva) were used to capture target proteins. eGFP tags were removed after tobacco etch virus protease digestion, which also cleaves the interdomain linkers in the ternary complex. Proteins were concentrated with ultrafiltration centrifugal devices of 50-kDa cutoff (Amicon, Millipore). Monodispersed fractions of proteins were collected from size-exclusion columns (Superdex 200 10/300 GL, GE Health Sciences) equilibrated with FPLC buffer (20 mM Hepes, pH 7.5, 150 mM NaCl, 1 mM n-dodecyl-β-D-maltopyranoside).

Soluble mouse cyt b_5 (1–89) and soluble mouse b_5R (30–301) were expressed in *Escherichia coli* (*E. coli*) BL21(DE3) as previously reported (44). Terrific broth media were supplemented with δ-aminolevulinic acid or riboflavin. Cobalt-based affinity resins (Talon, Clontech) were used to capture target proteins with an N-terminal His-tag, which was removed after tobacco etch virus protease digestion.

Production of ^{57}Fe-enriched SCD1

To remove Fe in commercial *FreeStyle 293* media, Chelex 100 chelating resins (Bio-Rad) were added at 20 g per 1 L and incubated under stirring at 4 °C for 5 days. Media were sterile-filtered after the treatment. $^{57}FeCl_3$ stock was prepared by dissolving ^{57}Fe powder (Isoflex) in 0.1 N HCl. Twenty millimolar of sterile-filtered $FeCl_3$ solution together with apo-transferrin was added to the treated media. Other essential divalent metal ions, including Mg^{2+} and Ca^{2+}, which were also removed by the chelating resins, were supplemented to the treated media per the previous report on the metal contents of *FreeStyle 293* media (63). The treated media were adjusted with NaOH or HCl to pH = 7.4. Despite the replenishment of essential metal ions, the treated media do not sustain the continuous growth of HEK cells. To minimize cell death, culture media were not changed until after viral transduction. About 16 h after viral transduction, cells in normal media were pelleted at 800×*g* and resuspended in the treated media with 10 mM sodium butyrate. Then, the suspended cells were incubated at 30 °C for 2 days before harvest. Purification was conducted as described above for the normal SCD1 sample.

Enzymatic assays of SCD1

Desaturation reactions of SCD1 with soluble cyt b_5 and b_5R were performed in conditions similar to those in previous reports (43, 44). SCD1 was mixed with 5-fold molar excess of soluble cyt b_5 and b_5R in FPLC buffer. Stearoyl-CoA (18:0) (Sigma) was used as substrate. For activity assays in liposomes, SCD1 was reconstituted into liver polar extract (Avanti) or brain polar extract lipids (Avanti) following a previous protocol (43). When testing the effects of transition metal ions, freshly prepared metal chloride salt stock solutions were added prior to the addition of NADH. Fe^{2+}, premixed with a sodium ascorbate stock, was added to achieve a final [ascorbate] of 100 μM and a desired [Fe^{2+}]. Reactions were initiated by the addition of 1 mM NADH. For the peroxide shunt reaction, only SCD1 and substrate stearoyl-CoA were included. H_2O_2 (Sigma) was added to start reactions. Aliquots of reaction mixtures were quenched at certain time points. Protein precipitates were pelleted by centrifugation. Supernatants containing acyl-CoAs were analyzed in HPLC. Calibration curves were generated from standard acyl-CoA samples. Initial rates were calculated from the linear fitting of time courses within the first 1 min for biological reactions with cyt b_5 and b_5R or within the first 5 min for peroxide shunt reactions. Relative activities were based on TTNs of reactions.

Inductively coupled plasma mass spectrometry

Protein samples for ICP-MS were collected from SEC with Superdex 75 10/300 GL column (GE Health Sciences) in which SCD1 with a detergent belt can be well separated from soluble cyt b_5 and b_5R. The FPLC buffer was prepared with deionized ultra-pure water, and O_2 in buffer was removed by three cycles of purging with Argon gas before the addition of detergent. One millimolar EDTA was added and incubated with samples for 10 min before loading into FPLC. The peak fractions of SCD1 were concentrated to ∼50 μM. Protein concentrations were determined by a protein colorimetric assay (Bio-Rad). Approximately 200 μL of proteins samples together with flow-through buffers (during concentration) as blank controls were accurately weighed and sent for ICP-MS (Agilent 8800 Triple Quad ICP-MS) analyses at the Department of Earth and Atmospheric Sciences of University of Houston. All protein samples were digested in 2% HNO_3. Calibrations with Fe, Zn, and Co standards were performed at the beginning and the end of each run. Metal contents of proteins were reported as the concentrations of metal in protein samples subtracted by those in the corresponding blank controls.

UV-Vis spectroscopy and anaerobic titration

UV-Vis spectra were recorded using a Hewlett-Packard 8453 diode-array spectrophotometer (Palo Alto). SCD1 solution in a tonometer was made anaerobic by 5 cycles of 30 s of vacuum followed by 4.5 min of saturating with argon. This anaerobic SCD1 solution was then titrated with anaerobic stock of dithionite in an air-tight syringe. The time courses of A_{340} in the reaction of H_2O_2 with SCD1 were recorded with an Applied Photophysics (Leatherhead) model SX-18MV stopped-flow instrument. The observed rates, k_{obs}, were obtained by fitting the time courses to biphasic exponential function. The fast spectral changes were monitored using the rapid-scan accessory with the stopped-flow machine, and the optical species were resolved using the Pro-Kinetics program provided by Applied Photophysics.

EPR spectroscopy

X-band EPR spectra were recorded with a Bruker EMX spectrometer (Billerica) operating at 10 K. A Bruker dual mode resonator was used, and the parameters for the EPR measurements were as follows: frequency, 9.58 GHz; microwave power, 4 mW; modulation frequency, 100 kHz; modulation amplitude, 10 G, and time constant, 0.33 s. The size of the EPR signals was based on peak-to-trough intensity. For power

dependence study, the range of microwave power ranged from 200 mW to 0.1 mW, with a step of 3 dB. To prepare Fe(II)/Fe(II) SCD1 in EPR tube, resting SCD1 after EPR measurement was thawed and the atmosphere above the solution was flushed with nitrogen (N_2) gas while small amount of dithionite was added to exhaust O_2 in the solution. The capped EPR tube was then transferred into an anaerobic chamber, and 1 μM deazaflavin and 1 mM EDTA were added to the anaerobic SCD1 solution. The sample was then irradiated with white light for 15 min before being frozen for EPR measurement.

Data availability

Data used for analyses are all included in the paper.

Supporting information—This article contains supporting information.

Acknowledgments—We acknowledge V. Berka for his help with the dithionite titration and G. Gerfen for insightful discussions on EPR data.

Author contributions—J. S., G. W., A.-L. T., and M. Z. conceptualization; J. S. and G. W. investigation; J. S., G. W., B. S. P., A.-L. T., and M. Z. methodology; J. S. and G. W. validation; J. S., G. W., and B. S. P. formal analysis; J. S., G. W., and M. Z. writing-original draft; J. S., G. W., B. S. P., A.-L. T., and M. Z. writing-review and editing; J. S. visualization; A.-L. T. and M. Z. supervision; A.-L. T. and M. Z. funding acquisition; B. S. P. data curation.

Funding and additional information—This work was supported by grants from NIH (DK122784 to M. Z. and A.-L. T). The content is solely the responsibility of the authors and does not necessarily represent the official views of the National Institutes of Health.

Conflict of interest—The authors declare that they have no conflicts of interest with the contents of this article.

Abbreviations—The abbreviations used are: AF, antiferromagnetic; eGFP, enhanced green fluorescent protein; EPR, electron paramagnetic resonance; FAD, flavin adenine dinucleotide; H_2O_2, hydrogen peroxide; HEK, human embryonic kidney; ICP-MS, inductively coupled plasma mass spectrometry; MUFAs, monounsaturated fatty acids; SCD, stearoyl-CoA desaturase; SEC, size-exclusion chromatography; TM, transmembrane; TTN, total turnover number.

References

1. Strittmatter, P., Spatz, L., Corcoran, D., Rogers, M. J., Setlow, B., and Redline, R. (1974) Purification and properties of rat liver microsomal stearyl coenzyme A desaturase. *Proc. Natl. Acad. Sci. U. S. A.* **71**, 4565–4569
2. Sperling, P., Ternes, P., Zank, T. K., and Heinz, E. (2003) The evolution of desaturases. *Prostaglandins Leukot. Essent. Fatty Acids* **68**, 73–95
3. Paton, C. M., and Ntambi, J. M. (2009) Biochemical and physiological function of stearoyl-CoA desaturase. *Am. J. Physiol. Endocrinol. Metab.* **297**, E28–E37
4. Wu, X., Zou, X., Chang, Q., Zhang, Y., Li, Y., Zhang, L., *et al.* (2013) The evolutionary pattern and the regulation of stearoyl-CoA desaturase genes. *Biomed. Res. Int.* **2013**, 856521
5. Evans, H., De Tomaso, T., Quail, M., Rogers, J., Gracey, A. Y., Cossins, A. R., *et al.* (2008) Ancient and modern duplication events and the evolution of stearoyl-CoA desaturases in teleost fishes. *Physiol. Genomics* **35**, 18–29
6. Ntambi, J. M., Miyazaki, M., Stoehr, J. P., Lan, H., Kendziorski, C. M., Yandell, B. S., *et al.* (2002) Loss of stearoyl-CoA desaturase-1 function protects mice against adiposity. *Proc. Natl. Acad. Sci. U. S. A.* **99**, 11482–11486
7. Gutiérrez-Juárez, R., Pocai, A., Mulas, C., Ono, H., Bhanot, S., Monia, B. P., *et al.* (2006) Critical role of stearoyl-CoA desaturase–1 (SCD1) in the onset of diet-induced hepatic insulin resistance. *J. Clin. Invest.* **116**, 1686–1695
8. Flowers, M. T., and Ntambi, J. M. (2008) Role of stearoyl-coenzyme a desaturase in regulating lipid metabolism. *Curr. Opin. Lipidol.* **19**, 248
9. Xin, Z., Zhao, H., Serby, M. D., Liu, B., Liu, M., Szczepankiewicz, B. G., *et al.* (2008) Discovery of piperidine-aryl urea-based stearoyl-CoA desaturase 1 inhibitors. *Bioorg. Med. Chem. Lett.* **18**, 4298–4302
10. Brown, J. M., and Rudel, L. L. (2010) Stearoyl-coenzyme A desaturase 1 inhibition and the metabolic syndrome: considerations for future drug discovery. *Curr. Opin. Lipidol.* **21**, 192–197
11. Oballa, R. M., Belair, L., Black, C. W., Bleasby, K., Chan, C., Desroches, C., *et al.* (2011) Development of a liver-targeted Stearoyl-CoA Desaturase (SCD) Inhibitor (MK-8245) to establish a therapeutic window for the treatment of diabetes and dyslipidemia. *J. Med. Chem.* **54**, 5082–5096
12. Zhang, Z., Dales, N. A., and Winther, M. D. (2014) Opportunities and challenges in developing stearoyl-coenzyme A desaturase-1 inhibitors as novel therapeutics for human disease. *J. Med. Chem.* **57**, 5039–5056
13. Sun, S., Zhang, Z., Raina, V., Pokrovskaia, N., Hou, D., Namdari, R., *et al.* (2014) Discovery of thiazolylpyridinone SCD1 inhibitors with preferential liver distribution and reduced mechanism-based adverse effects. *Bioorg. Med. Chem. Lett.* **24**, 526–531
14. Sun, S., Zhang, Z., Kodumuru, V., Pokrovskaia, N., Fonarev, J., Jia, Q., *et al.* (2014) Systematic evaluation of amide bioisosteres leading to the discovery of novel and potent thiazolylimidazolidinone inhibitors of SCD1 for the treatment of metabolic diseases. *Bioorg. Med. Chem. Lett.* **24**, 520–525
15. Aljohani, A. M., Syed, D. N., and Ntambi, J. M. (2017) Insights into Stearoyl-CoA Desaturase-1 Regulation of Systemic Metabolism. *Trends Endocrinol. Metab.* **28**, 831–842
16. Fritz, V., Benfodda, Z., Rodier, G., Henriquet, C., Iborra, F., Avances, C., *et al.* (2010) Abrogation of de novo lipogenesis by stearoyl-CoA desaturase 1 inhibition interferes with oncogenic signaling and blocks prostate cancer progression in mice. *Mol. Cancer Ther.* **9**, 1740–1754
17. Peck, B., Schug, Z. T., Zhang, Q., Dankworth, B., Jones, D. T., Smethurst, E., *et al.* (2016) Inhibition of fatty acid desaturation is detrimental to cancer cell survival in metabolically compromised environments. *Cancer Metab.* **4**, 6
18. Vriens, K., Christen, S., Parik, S., Broekaert, D., Yoshinaga, K., Talebi, A., *et al.* (2019) Evidence for an alternative fatty acid desaturation pathway increasing cancer plasticity. *Nature* **566**, 403–406
19. Oatman, N., Dasgupta, N., Arora, P., Choi, K., Gawali, M. V., Gupta, N., *et al.* (2021) Mechanisms of stearoyl CoA desaturase inhibitor sensitivity and acquired resistance in cancer. *Sci. Adv.* **7**, eabd7459
20. Peck, B., and Schulze, A. (2016) Lipid desaturation - the next step in targeting lipogenesis in cancer? *FEBS J.* **283**, 2767–2778
21. Magtanong, L., Ko, P. J., To, M., Cao, J. Y., Forcina, G. C., Tarangelo, A., *et al.* (2019) Exogenous monounsaturated fatty acids promote a ferroptosis-resistant cell state. *Cell Chem. Biol.* **26**, 420–432.e9
22. Tesfay, L., Paul, B. T., Konstorum, A., Deng, Z., Cox, A. O., Lee, J., *et al.* (2019) Stearoyl-CoA Desaturase 1 protects ovarian cancer cells from ferroptotic cell death. *Cancer Res.* **79**, 5355–5366
23. Luis, G., Godfroid, A., Nishiumi, S., Cimino, J., Blacher, S., Maquoi, E., *et al.* (2021) Tumor resistance to ferroptosis driven by Stearoyl-CoA Desaturase-1 (SCD1) in cancer cells and Fatty Acid Biding Protein-4 (FABP4) in tumor microenvironment promote tumor recurrence. *Redox Biol.* **43**, 102006

24. Yahagi, N., Shimano, H., Hasegawa, K., Ohashi, K., Matsuzaka, T., Najima, Y., *et al.* (2005) Co-ordinate activation of lipogenic enzymes in hepatocellular carcinoma. *Eur. J. Cancer* **41**, 1316–1322
25. Scaglia, N., and Igal, R. A. (2008) Inhibition of Stearoyl-CoA desaturase 1 expression in human lung adenocarcinoma cells impairs tumorigenesis. *Int. J. Oncol.* **33**, 839–850
26. Scaglia, N., Chisholm, J. W., and Igal, R. A. (2009) Inhibition of stearoylCoA desaturase-1 inactivates acetyl-CoA carboxylase and impairs proliferation in cancer cells: role of AMPK. *PLoS One* **4**, e6812
27. Ackerman, D., and Simon, M. C. (2014) Hypoxia, lipids, and cancer: surviving the harsh tumor microenvironment. *Trends Cell Biol.* **24**, 472–478
28. Theodoropoulos, P. C., Gonzales, S. S., Winterton, S. E., Rodriguez-Navas, C., McKnight, J. S., Morlock, L. K., *et al.* (2016) Discovery of tumor-specific irreversible inhibitors of stearoyl CoA desaturase. *Nat. Chem. Biol.* **12**, 218–225
29. Savino, A. M., Fernandes, S. I., Olivares, O., Zemlyansky, A., Cousins, A., Markert, E. K., *et al.* (2020) Metabolic adaptation of acute lymphoblastic leukemia to the central nervous system microenvironment is dependent on Stearoyl CoA desaturase. *Nat. Cancer* **1**, 998–1009
30. Vincent, B. M., Tardiff, D. F., Piotrowski, J. S., Aron, R., Lucas, M. C., Chung, C. Y., *et al.* (2018) Inhibiting Stearoyl-CoA Desaturase Ameliorates alpha-Synuclein Cytotoxicity. *Cell Rep.* **25**, 2742–2754.e31
31. Fanning, S., Haque, A., Imberdis, T., Baru, V., Barrasa, M. I., Nuber, S., *et al.* (2019) Lipidomic analysis of alpha-Synuclein Neurotoxicity Identifies Stearoyl CoA Desaturase as a target for parkinson treatment. *Mol. Cell* **73**, 1001–10014.e8
32. Nuber, S., Nam, A. Y., Rajsombath, M. M., Cirka, H., Hronowski, X., Wang, J., *et al.* (2021) A Stearoyl-Coenzyme A Desaturase Inhibitor Prevents Multiple Parkinson Disease Phenotypes in alpha-Synuclein Mice. *Ann. Neurol.* **89**, 74–90
33. Hamilton, L. K., Moquin-Beaudry, G., Mangahas, C. L., Pratesi, F., Aubin, M., Aumont, A., *et al.* (2022) Stearoyl-CoA Desaturase inhibition reverses immune, synaptic and cognitive impairments in an Alzheimer's disease mouse model. *Nat. Commun.* **13**, 2061
34. Vergeres, G., and Waskell, L. (1995) Cytochrome b_5, its functions, structure and membrane topology. *Biochimie* **77**, 604–620
35. Spatz, L., and Strittmatter, P. (1973) A form of reduced nicotinamide adenine dinucleotide-cytochrome b5 reductase containing both the catalytic site and an additional hydrophobic membrane-binding segment. *J. Biol. Chem.* **248**, 793–799
36. Rogers, M. J., and Strittmatter, P. (1975) The interaction of NADH-cytochrome b_5 reductase and cytochrome b_5 bound to egg lecithin liposomes. *J. Biol. Chem.* **250**, 5713–5718
37. Iyanagi, T. (1977) Redox properties of microsomal reduced nicotinamide adenine dinucleotide-cytochrome b5 reductase and cytochrome b5. *Biochemistry* **16**, 2725–2730
38. Iyanagi, T., Watanabe, S., and Anan, K. F. (1984) One-electron oxidation-reduction properties of hepatic NADH-cytochrome b5 reductase. *Biochemistry* **23**, 1418–1425
39. Yamada, M., Tamada, T., Takeda, K., Matsumoto, F., Ohno, H., Kosugi, M., *et al.* (2013) Elucidations of the Catalytic Cycle of NADH-Cytochrome b_5 Reductase by X-ray Crystallography: new insights into regulation of efficient electron transfer. *J. Mol. Biol.* **425**, 4295–4306
40. Man, W. C., Miyazaki, M., Chu, K., and Ntambi, J. M. (2006) Membrane topology of mouse stearoyl-CoA desaturase 1. *J. Biol. Chem.* **281**, 1251–1260
41. Bai, Y., McCoy, J. G., Levin, E. J., Sobrado, P., Rajashankar, K. R., Fox, B. G., *et al.* (2015) X-ray structure of a mammalian stearoyl-CoA desaturase. *Nature* **524**, 252–256
42. Wang, H., Klein, M. G., Zou, H., Lane, W., Snell, G., Levin, I., *et al.* (2015) Crystal structure of human stearoyl-coenzyme A desaturase in complex with substrate. *Nat. Struct. Mol. Biol.* **22**, 581–585
43. Shen, J., Wu, G., Tsai, A. L., and Zhou, M. (2022) Transmembrane helices mediate the formation of a stable ternary complex of b5R, cyt b5, and SCD1. *Commun. Biol.* **5**, 956
44. Shen, J., Wu, G., Tsai, A. L., and Zhou, M. (2020) Structure and mechanism of a unique diiron center in mammalian Stearoyl-CoA Desaturase. *J. Mol. Biol.* **432**, 5152–5161
45. Lindqvist, Y., Huang, W., Schneider, G., and Shanklin, J. (1996) Crystal structure of delta9 stearoyl-acyl carrier protein desaturase from castor seed and its relationship to other di-iron proteins. *EMBO J* **15**, 4081–4092
46. Högbom, M., Huque, Y., Sjöberg, B.-M., and Nordlund, P. (2002) Crystal structure of the di-iron/radical protein of ribonucleotide reductase from Corynebacterium ammoniagenes. *Biochemistry* **41**, 1381–1389
47. Sazinsky, M. H., and Lippard, S. J. (2006) Correlating structure with function in bacterial multicomponent monooxygenases and related diiron proteins. *Acc. Chem. Res.* **39**, 558–566
48. Jasniewski, A. J., and Que, L., Jr. (2018) Dioxygen activation by nonheme diiron enzymes: diverse dioxygen adducts, high-valent intermediates, and related model complexes. *Chem. Rev.* **118**, 2554–2592
49. Shanklin, J., Whittle, E., and Fox, B. G. (1994) Eight histidine residues are catalytically essential in a membrane-associated iron enzyme, stearoyl-CoA desaturase, and are conserved in alkane hydroxylase and xylene monooxygenase. *Biochemistry* **33**, 12787–12794
50. Zhu, G., Koszelak-Rosenblum, M., Connelly, S. M., Dumont, M. E., and Malkowski, M. G. (2015) The crystal structure of an integral membrane fatty acid alpha-Hydroxylase. *J. Biol. Chem.* **290**, 29820–29833
51. Joshi, V. C., Wilson, A. C., and Wakil, S. J. (1977) Assay for the terminal enzyme of the stearoyl coenzyme A desaturase system using chick embryo liver microsomes. *J. Lipid Res.* **18**, 32–36
52. Bailey, L. J., and Fox, B. G. (2009) Crystallographic and catalytic studies of the peroxide-shunt reaction in a diiron hydroxylase. *Biochemistry* **48**, 8932–8939
53. Guzov, V. M., Houston, H. L., Murataliev, M. B., Walker, F. A., and Feyereisen, R. (1996) Molecular cloning, overexpression in Escherichia coli, structural and functional characterization of house fly cytochrome b5. *J. Biol. Chem.* **271**, 26637–26645
54. Yu, M.-J., and Chen, S.-L. (2019) From Alkane to Alkene: the inert Aliphatic C–H Bond activation presented by binuclear Iron Stearoyl-CoA Desaturase with a Long di-Fe Distance of 6 Å. *ACS Catal.* **9**, 4345–4359
55. Gray, H. B., and Winkler, J. R. (2018) Living with oxygen. *Acc. Chem. Res.* **51**, 1850–1857
56. Esselborn, J., Kertess, L., Apfel, U. P., Hofmann, E., and Happe, T. (2019) Loss of specific active-site iron atoms in Oxygen-Exposed [FeFe]-Hydrogenase determined by detailed X-ray structure analyses. *J. Am. Chem. Soc.* **141**, 17721–17728
57. Wu, G., Rogge, C. E., Wang, J. S., Kulmacz, R. J., Palmer, G., and Tsai, A. L. (2007) Oxyferryl heme and not tyrosyl radical is the likely culprit in prostaglandin H synthase-1 peroxidase inactivation. *Biochemistry* **46**, 534–542
58. Xia, Y., Tsai, A. L., Berka, V., and Zweier, J. L. (1998) Superoxide generation from endothelial nitric-oxide synthase. A Ca2+/calmodulin-dependent and tetrahydrobiopterin regulatory process. *J. Biol. Chem.* **273**, 25804–25808
59. Berka, V., Wu, G., Yeh, H. C., Palmer, G., and Tsai, A. L. (2004) Three different oxygen-induced radical species in endothelial nitric-oxide synthase oxygenase domain under regulation by L-arginine and tetrahydrobiopterin. *J. Biol. Chem.* **279**, 32243–32251
60. Hider, R. C., and Kong, X. L. (2011) Glutathione: a key component of the cytoplasmic labile iron pool. *Biometals* **24**, 1179–1187
61. Cabantchik, Z. I. (2014) Labile iron in cells and body fluids: physiology, pathology, and pharmacology. *Front. Pharmacol.* **5**, 45
62. Goehring, A., Lee, C.-H. H., Wang, K. H., Michel, J. C., Claxton, D. P., Baconguis, I., *et al.* (2014) Screening and large-scale expression of membrane proteins in mammalian cells for structural studies. *Nat. Protoc.* **9**, 2574–2585
63. Richardson, C. E. R., Cunden, L. S., Butty, V. L., Nolan, E. M., Lippard, S. J., and Shoulders, M. D. (2018) A method for selective depletion of Zn(II) Ions from complex biological media and evaluation of cellular consequences of Zn(II) deficiency. *J. Am. Chem. Soc.* **140**, 2413–2416